Detecting Glacier Surface Motion by Optical Flow

M.G. Lenzano, E. Lannutti, C. Toth, A. Rivera, and L. Lenzano

Abstract

In this study, we assessed the feasibility of using optical flow, in particular, large displacement optical flow (LDOF) method as a possible solution to obtain surface movement data to derive ice flow velocities in a glacier. Tests were carried out at the Viedma Glacier, located at the South Patagonia Icefield, Argentina, where terrestrial monoscopic image sequences were acquired by a calibrated camera from April 2014 until April 2016. As for preprocessing, the Correlated Analysis method was implemented to avoid and minimize errors due to the measurable changes in lighting, shadows, clouds, and snow. The results show a flow field with a maximum surface velocity value of 3.5 m/d. The errors were minimized by averaging the image sequence results based on seasons, in which the Total Error Reconstruction yielded fairly good mean accuracy (0.36 m/d). In summary, it was demonstrated that LDOF can provide accurate and robust solution to detect daily changes in the glacier surface.

Introduction

Geospatial data acquisition methods for Earth observation and monitoring applications have seen great technological advancements in recent years (Bartholomé and Belward, 2005), as the performance potential of the sensors, in terms of spatial, spectral, and temporal resolutions has significantly expanded. Consequently, nowadays remote sensing techniques represent an attractive and affordable approach to study different natural phenomena, such as glaciers, where the main advantage is a simpler and more economical implementation compared to conventional field surveying measurements. At present, optical imagery is the most commonly used sensory data to monitor glaciers because it is an efficient low cost method, used since mid-1980s for mapping surface velocities. (Heid and Kääb, 2012).

To study glaciers, a variety of methods and techniques have been used since the mid-nineteenth century (Gao and Liu, 2001; Bamber and Rivera, 2007); typically a combination of these is required to obtain high resolution spatial and temporal observations needed to model the complexity of the dynamics processes. Airborne/spaceborne remote sensing easily provides consistently accurate low and medium resolution data over large areas (Toth and Jóźków, 2016). In contrast, terrestrial or close-range sensors (Moustafa, 2000) can provide high resolution observations (Schwalbe *et al.*, 2016), and thus difficult to map topographies, such as glaciers, can be surveyed with high accuracy for smaller areas. Satellite-based optical sensors may often have limiting factors for observations, such as cloud cover, especially in mountain regions (Gleitsmann and Kappas, 2006). Since glaciers are dynamic objects, the temporal aspects of the mapping are equally important, and therefore, the revisit time of satellite platforms may present some disadvantages. A permanent sensor installation could offer unprecedented temporal resolution and observation capabilities (Toth and Jóźków, 2016), and using time-lapse imagery provides a viable approach to glacier change detection (Harrison, 1992; Hashimoto *et al.*, 2009; Ahn and Box, 2010; Maas *et al*, 2010; Rivera *et al.*, 2012b; Danielson and Sharp, 2013; Lenzano *et al.*, 2014).

The dynamics of glaciers has noticeably changed due to global warming during in the late 20th and 21st centuries (Oerlemans, 2005; Bolch *et al.*, 2012), and thus, to properly assess and monitor their dynamics requires the detailed mapping of surface velocities and changes in geometry (Howat *et al.*, 2007); noted that subsurface velocities are also of importance, but they cannot be easily observed. Ice flow velocities vary along glaciers, following complex patterns defined by stress and strain rate distributions (Benn and Evans, 2010). In order to map glacier surface velocities, various methods have been used, including traditional point-based surveys, and then using remote sensing methods that can provide mass points in irregular or regular grid distributions. Photogrammetric and computer vision methods are available to obtain a dense and accurate grid adequate to support glacier dynamic analysis (Matías *et al.*, 2009; Westoby *et al.*, 2012; Ryan *et al.*, 2015, Piermattei *et al.*, 2015), and may provide various metric products, such as ice velocities, volume changes, etc. Note that photogrammetry is fundamentally concerned about the metric integrity of the derived products, while computer vision is primarily focused on the correct recognition and reconstruction of objects. Clearly, photogrammetry and computer vision share, or at least should share, a common (or at least widely overlapping) theoretical basis (Granshaw and Fraser, 2015). Certainly, exploiting the complementarities of the two disciplines may provide accurate solutions to monitoring many natural phenomena.

Image sequence processing in computer vision is a broad field, and includes tracking, structure from motion (SFM), optical flow, etc. These subfields are closely related, and the concept is that the object/observer movement enables to obtain accurate information of the sensed changes over time, which is mostly based on identifying conjugate geometrical primitives in the images. Finding correspondence between pairs of points in two images remains one of the fundamental computational challenges in computer vision (Wedel *et al.*, 2009). At the beginning of the 1980's, techniques based on coarse-to-fine strategies were developed, such as intensity-based optical flow algorithms, and then quantitative methods of computer vision, including many early feature-based stereo correspondence algorithms (Szelisky, 2010). In some cases, different motion and structure paradigms were developed, using optical flow as an intermediate representation of motion correspondences between image features, correlations, or properties of intensity structures (Beauchemin and Barron,

M.G. Lenzano, E. Lannutti, and L. Lenzano are with the Departamento de Geomática. Instituto Argentino de Nivología, Glaciología y Ciencias Ambientales-CCT, CONICET, Mendoza, Argentina. Casilla de correo 300, Av. Ruiz Leal s/n. Parque Gral. San Martín. Mendoza. Argentina. CP: 5500. (mlenzano@mendoza-conicet.gob.ar).

C. Toth is with the Department of Civil, Environmental and Geodetic Engineering, The Ohio State University, Ohio, USA. 470 Hitchcock Hall, 2070 Neil Ave., Columbus, OH 43210

A. Rivera is with Centro de Estudios Científicos de Chile, Valdivia, Chile. Arturo Prat 514, Valdivia, Chile.

Photogrammetric Engineering & Remote Sensing
Vol. 84, No. 1, January 2018, pp. 33–42.
0099-1112/17/33–42

doi: 10.14358/PERS.84.1.33

1995). The optical flow extracted from imagery is the result of the apparent movement pattern between objects, caused by either relative deformation or absolute movements. The objective of motion estimation is to compute an independent estimate of motion for each pixel, which is generally known as optical flow (Szelisky, 2010). Optical flow-based methods can be classified as differential, correlation, frequency, and variational (De la Nuez, 2010). The variational methods have demonstrated the best performance, allowing the accurate estimation of dense flow field based on the original formulation, introduced by Horn and Schunck (1981).

In spite of the existence of a variety of optical flow techniques, the majority of the algorithms concern small displacements and only a few procedures have been developed to detect large displacements, such as work by Weinzaepfel *et al.* (2013). With respect to the image acquisition rate, changes occurring in time-lapse images of glaciers, where for half of the day no imagery can be acquired, the changing displacement could be large. The Large Displacement Optical Flow (LDOF) method (Brox *et al.*, 2004; Brox *et al.*, 2009; Brox and Malik, 2011) offers a powerful solution to estimate large displacements in image sequences, and is based on a solid numerical method that combines descriptor matching with the variational model, and uses a coarse-to-fine strategy with the so-called warping technique. Finally, the descriptor matching and the discrete optimizations can provide sub-pixel accuracy.

Only a few studies of ice motion have been carried out using optical flow algorithm, such as using satellite and terrestrial images by (Vogel *et al.*, 2012) and (Bown, 2015), respectively. In this work, we propose to use the LDOF algorithm to estimate the glacier motion based on terrestrial, monoscopic time-lapse image series, acquired by non-metric professional DSLR cameras systems. The optical flow method from computer vision will provide the change detection of 3D objects, and the photogrammetric processes will supply the scaling and the metric characterization of the glacier movement. This study aims to obtain accurate solutions at pixel level with high temporal and spatial resolution, and determine ice velocities of the glacier terminus. The test was carried out at the Viedma glacier, Southern Patagonia Icefield (SPI), Argentina between 2014 and 2016. This site is an important calving glacier in the region covering an area of 945 km^2 (Aniya *et al.*, 1996). Since the behavior of the glacier at the terminus is of high interest, this area was selected for the investigation. The investigation is a continuation of our previous effort (Lannutti *et al.*, 2016; Toth *et al.*, 2016). The outline of this paper is as follows: the next Section provides a detailed description of the study area and data collection, followed by a review of the methodology proposed. Then, the results with analysis is provided leading to the conclusions.

Test Area and Data Acquisition

The South Patagonia Ice field (SPI) is located in South America, Argentina and Chile, covering an area of 13,000 km^2 with an average length of approximately 30 to 40 km at a mean altitude of 1,191 m ASL (Aniya, 2013). Viedma glacier is located at 49° 31′ S, 72° 59′ W, Los Glaciares National Park, SPI, Santa Cruz, Argentina, see Figure 1. The glacier was selected for this study due to the availability of earlier investigations, carried out over the past 30 years (Skvarca *et al.*, 1995; Aniya *et al.*, 1996; Lopez *et al.*, 2010; Riveros *et al.*, 2013), and its representativeness at the SPI.

To support the field image acquisition of the time-lapse imagery, an integrated data acquisition system was built based on a CANON EOS Mark II DSLR camera (C1); pixel size: 7.2 µm, objective focal length: 50 mm, and FOV: 46°. The C1 was calibrated prior to field deployment by the United States Geological Survey (USGS). Also, a NIKON D3 camera (C2) calibrated by Rollei Metric was used for preprocessing purposes; pixel size: 8.5 µm, objective focal length: 35 mm, and FOV: 62°. Both systems are powered by one 12V/7Ah lead acid battery, charged by two 38W solar panels. The cameras with the supporting electronic systems are protected by a waterproof box with a visor to reduce reflections. An inspection port in the rear of the enclosure provides visual access for monitoring the camera operation. The image acquisition systems were installed on a rigid metal structure, fixed to outcrops of the south margin of the Viedma Glacier. The C1 was located 70 m

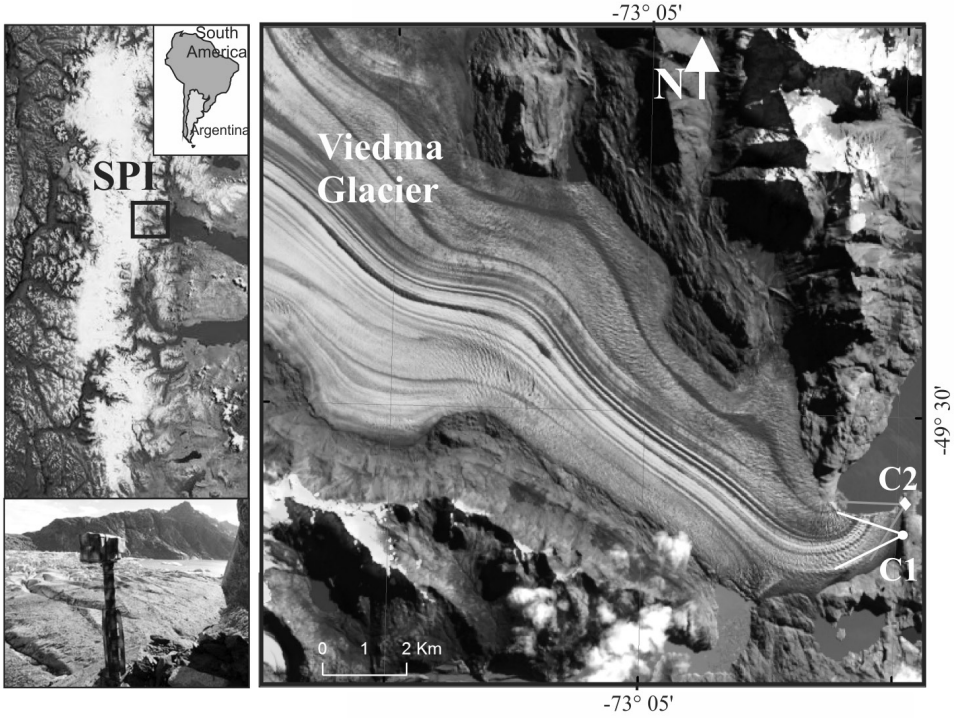

Figure 1. Map of the study area with each camera location and FOV.

above the glacier surface from where a good side view of the curving glacier is provided, while C2 was placed to look at the front of the glacier, see Figure 1. Although the cameras are subject to short term disturbances by buffeting wind, the used platforms are robust enough for limiting sensor movements. Data acquisition in both systems started on 17 April 2014, and lasted until 17 April 2016 (in total, 605 images were selected and subsequently used for processing). The images were captured at 12:00 pm local time, generally coinciding with the highest position of the sun.

Field Support Data

In order to relate the image space to the object space, a number of primary Ground Control Points (*p*GCPs) visible within the camera views (C1 and C2) were surveyed. Dual-frequency Trimble 5700 GPS receivers were used to measure 11 *p*GCPs, seven and four in the FOV of C1 and C2, respectively, selected from a variety of topographic features, including rock outcrops and erratic blocks since they were static in relation to the glacier motion during the study period. The GPS measurements were referenced to the CHLT (Chaltén) CORS station, located at El Chaltén. Using DGPS static positioning method, the data were processed using the RtkLib open-source software (Wiśniewski *et al.*, 2013), with fixed solutions at the 95 percent confidence level. The RMSEs (root-mean-square error) for the GCPs were N = 0.01 m, E = 0.01 m, and U= 0.025 m, respectively.

Proposed Method

The overall processing workflow is shown in Figure 2; all the algorithms and data handling processes were implemented in Matlab. During preprocessing, the images are prepared and optimized for the optical flow computation. In addition, using the calibration parameters, the lens distortion is removed from the images. In order to reduce computational costs, the original image size of C1 camera was reduced by about 30 percent based on the actual Region of Interest (ROI); the glacier area was kept and the sky and background mountain range at the top of the photos were eliminated. The External Orientation Parameters (EOPs) for C1 and C2 cameras were calculated. To add more ground control data to support the scaling of the optical flow results, in addition of the surveyed by GPS (*p*GCPs), secondary GCPs, obtained by the stereo resection using images from both cameras, were introduced. Then, the main processing component, the optical flow computation method is executed, including the Correlation Analysis process based on RGB components and the LDOF computation that also provides the uncertainty estimation. Finally, as postprocessing, the results were scaled to provide object space parameters for the glaciological interpretations.

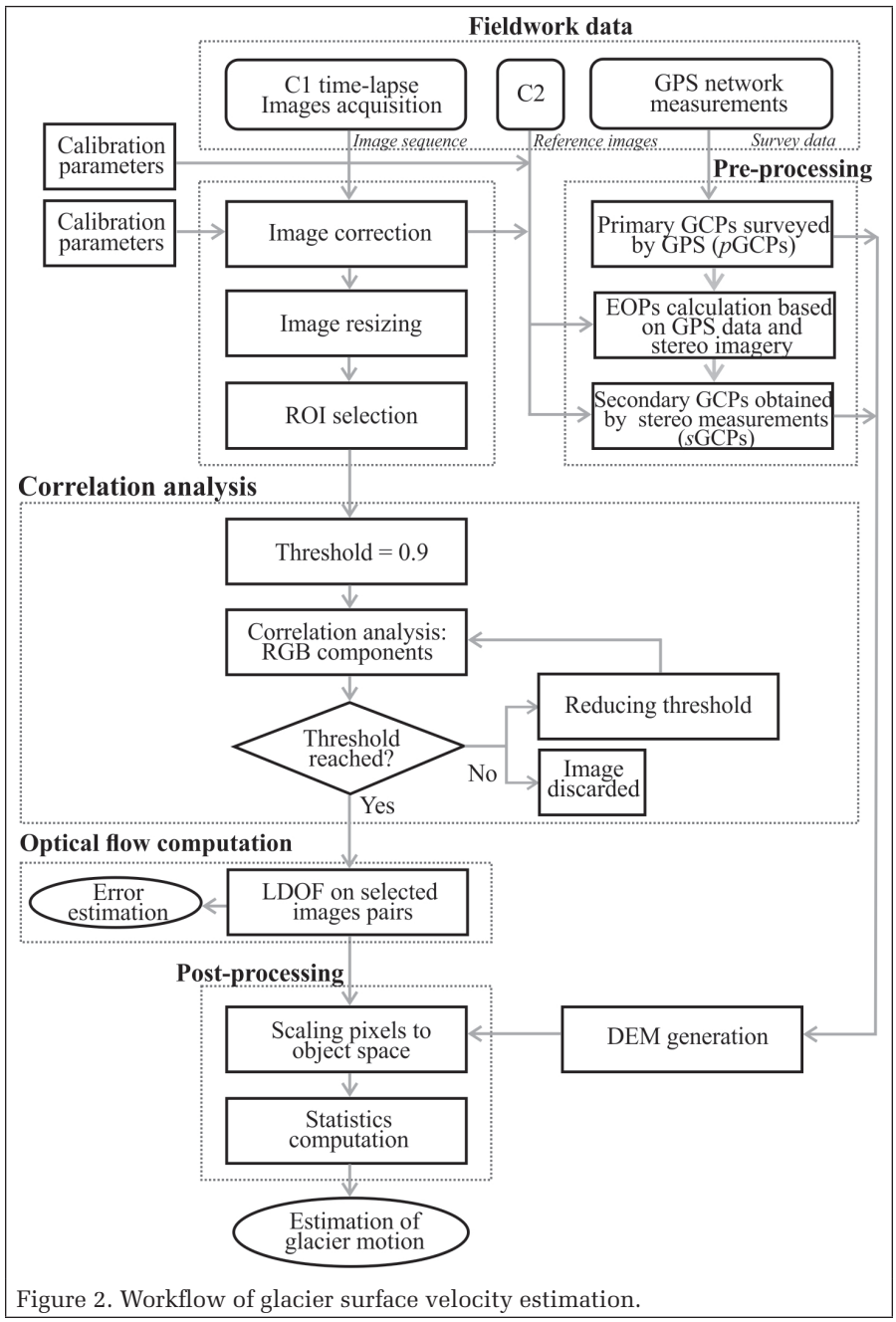

Figure 2. Workflow of glacier surface velocity estimation.

Image Correction and Orientation

To obtain the highest accuracy of any derived geospatial product, the imaging sensor must be calibrated and oriented as accurately as feasible. Interior and exterior orientation parameters that model the camera geometry and the relationship between the camera and object reference systems must be computed using features previously matched in both spaces (Garcia Tomaselli and Lopes Reiss, 2005). How closely the model conforms to reality will depend on the model and how well the parameters of the model can be estimated (Clarke and Fryer, 1998). The parameters that describe the physical model of a camera can be grouped into two categories. The first group, defined by linear parameters, includes the focal length, pixel size, and coordinates of the principal point. The lens distortion modeling is based on nonlinear parameters, including multiple parameters. For most cameras, the radial and, with less importance, decentering components provide adequate corrections, and are parametrized by (k_1, k_2, k_3) and (p_1 and p_2) polynomial coefficients, respectively. Note that lens distortions could have an increasingly adverse impact on accuracy with increasing target distance. In this study, both cameras were

accurately calibrated before field deployment, and linear as well as radial and tangential correction were applied to all the images to mitigate the lens distortion.

The EOP describe the orientation, three rotation angles ω,φ,κ, and position, X, Y, Z coordinates, of the camera with respect to a reference system, and thus connecting the imaging/camera frame to an object space frame. The estimation of the EOPs can be accomplished many ways. Here the sensor installation locations (C1 and C2) were known from GPS surveys, so mainly, the orientation angles had to be estimated based on using *p*GCPs. The single photo resection (SPR) problem is solved through a point-based approach, where at least three non-collinear conjugate points, i.e., targeted control points, are used in a least-squares adjustment based on the well-known collinearity equations (Lichti *et al.*, 2009). In this study, the camera positions were also calculated by the Perspective-Three-Point (P3P) approach that determines the pose of the camera from three correspondences between 3D target points and their 2D projections; the implementation by Kneip *et al.* (2011) was used.

GCP Densification Using Stereo Imagery (sGCPs)

To scale the optical flow results, additional ground control is needed to the previous *p*GCPs, such as, ideally, an accurate Digital Elevation Model (DEM). Thus, to generate a reasonable DEM, it is necessary to have a representative sample of 3D points evenly distributed in the image frame. In lieu of a surface model, sample points, sort of secondary GCPs, can be used, which can be obtained by the stereo intersection using the C1 and C2 images. During that process, lines of sight from each camera to the same point on the ice were identified on nearly simultaneously acquired image pairs from both cameras, and then approximate location of these points was computed. Since the base/height (B/H) ratio is rather small, multiple resections were performed, so the 3D positions could be averaged to improve accuracy; note that the base was 805 m and the depth was 2,000+ m on average. In total, 43 fairly evenly distributed surface points were extracted with an estimated accuracy of 0.2 m (Chang *et al.*, 1992).

Correlation Analysis (CA)

The grey value consistency assumption is a fundamental to optical flow estimation. Natural scenes observed by a static sensor, in general, always experience changes in brightness that may make the optical flow calculation challenging. Therefore, using the image gradient instead of the intensity value (Tistarelli, 1994) allows for small variations in the grey value, making the estimation of the relationship between surface motion and the image brightness changes more reliable. This concept assumes that the observed brightness/intensity gradient of any object is constant over time, and any change in value at a point is due to the motion (Kearney *et al.*, 1987). In addition to the gradient constraint, there is another assumption that nearby points in the image moves in a similar way (Schalkoff, 1989). Consequently, noticeable changes in lighting should be avoided to assure that changes of image intensity between images are only caused by motion in the object space (Klette, 2014). To assess the differences between two images, the summation of color differences between corresponding pixels over the image is performed. Figure 3a shows the RGB intensity distributions for different images acquired under varying conditions, including clear day without snow cover, a cloudy day without snow cover, a clear day with snow cover, and a cloudy day with snow cover. These changes, mainly due to solar radiation and seasonal snow, can significantly impact the optical flow computation. In our study case, the daily lightness changes were analyzed and images that were markedly different were removed by the CA.

Initially, the first image pair is selected from the time-lapse image series, IM_n (Master) and IS_{n+1} (Slave). It should be emphasized that the *IM* was selected taking into account the optimal contrast and lightness characteristics of the glacier surface, and afterwards, the filter (CA) may select images with similar conditions. Then, the histogram for each RGB band is separately computed for both images. Next, the mean correlation value for each of the three channels is analyzed. If the mean value is equal or greater than 0.90, then the pair remains selected. Otherwise, the computation starts again, and a new correlation between the IM_n and the IS_{n+2} is calculated with the threshold of 0.90 iteratively reduced by 0.007 in each step. The process will stop when the mean is greater than the descending correlation threshold, and the new pair is selected. The value of 0.007 was chosen by experimentally tests; for example, having a larger step will allow for a lower correlation between pairs. In the worst case, the images are separated by 40 days in time; see the 425 to 465 images in Figure 3b. Clearly, the variation of the threshold to pass depends on how dissimilar the light conditions in the RGB channels are in the image pairs. The process is repeated until all the images have been processed; IS_{n+m} becomes IM_{n+m}, where m defines which will be the next image master. In natural environment, such as glaciers, the objects may change substantially over longer time due to the glacier's movement, but in shorter time, such as a few weeks, the motion is likely exhibiting a similar pattern. Therefore, losing a few consecutive image pairs has limited impact on the motion estimation. Obviously, there is a practical time limit beyond which it may not be possible to identify corresponding objects. As a result of filtering, the original time-lapse image sequence is reduced to a subset of images where the changes in luminosity are relatively small, and thus the selected pairs should be likely processed successfully in the LDOF computation.

Figure 3b shows the intermediate and final results of the CA. The blue line describes the correlation value for the mean value of the three RGB bands for the *n-1* image pairs. The black line corresponds to the threshold of the iterative correlation test that decreases until it coincides with the RGB correlation value, and hence the test is passed. The dark points show the 231 image pairs selected by the CA, i.e., 38 percent of the images passed the test. The lowest threshold value for the 40 days apart case was 0.59. Clearly, this is the worst situation, coinciding with a major snow cover and changing weather conditions. The best case was with one day of difference with a correlation value of 0.99.

Optical Flow (LDOF)

We use the LDOF Matlab implementation developed by Brox *et al.* (2004), Brox and Malik (2011) (*https://www.cs.cmu.edu/~katef/*LDOF*.html*). Several other optical flow algorithms, such as the Scale-Invariant Feature Transformation (SIFT) based flow developed by Liu (2009) that establishes dense, semantically meaningful correspondence between two images across scenes by matching pixel-wise, or the Pyramidal implementation of the Lucas Kanade Feature Tracker algorithm (Bouguet, 2001) were also tested. Based on the comparisons, the LDOF produced the best motion estimation results for our datasets. This algorithm implements a coarse-to-fine variational framework between two images I_1 and I_2 and computes the displacement field by minimizing the functional energy *E(w)* using the following model (Equation 1). This method is based on energy minimization that penalizes the deviation in relation to the constraints imposed on the model.

$$E(w)=E_{color}(w)+\gamma E_{gradient}(w)+\alpha E_{smooth}(w)+\beta E_{match}(w, w_1)+E_{desc}(w_1) \quad (1)$$

where: α, β and γ are tuning parameters which can be determined manually according to qualitative evidence based on a large variety of images, or can be estimated automatically from ground truth data. These three parameters were experimentally determined by varying their ranges until optimal

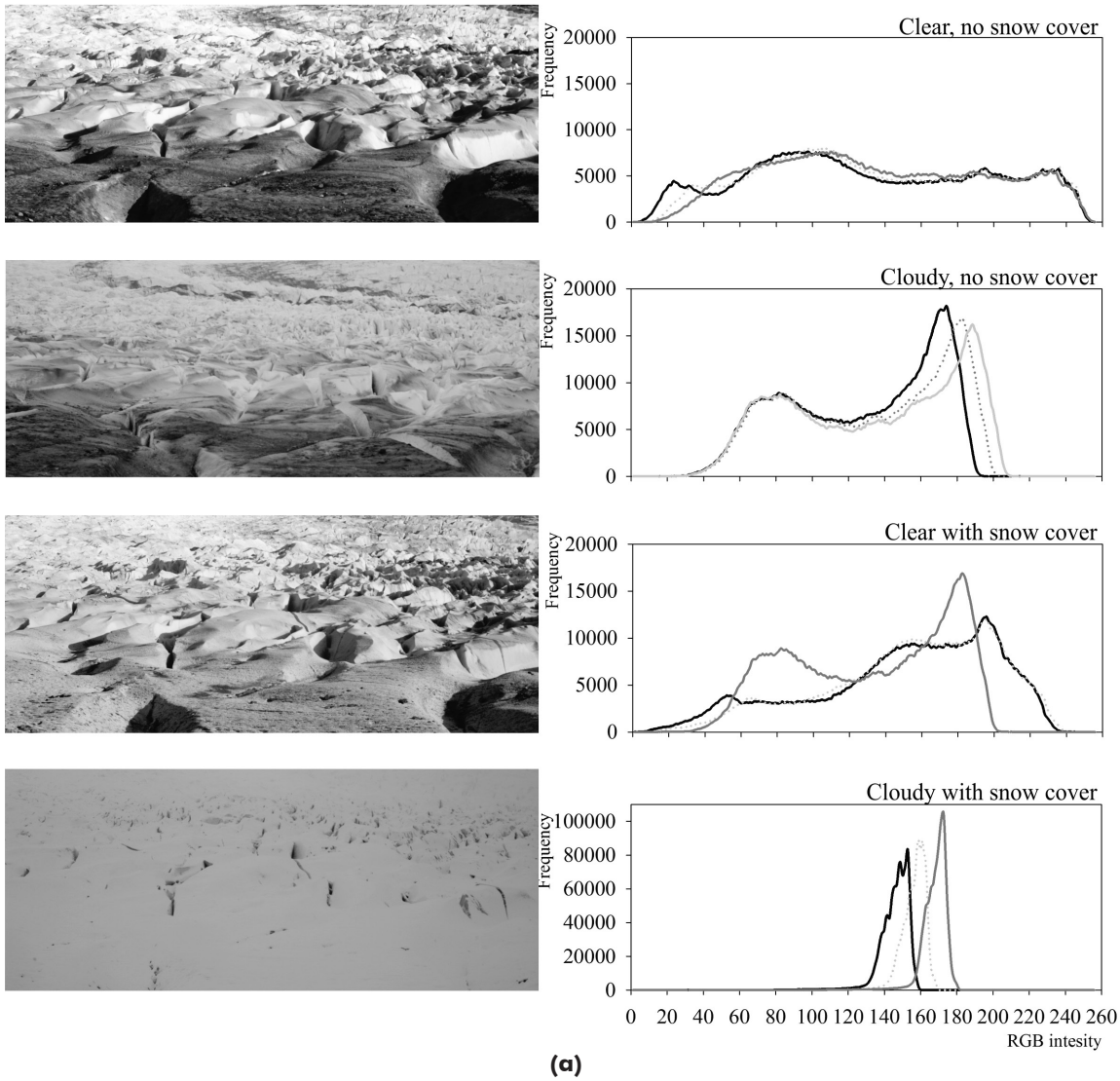

Figure 3. (a) Examples for daily changes in RGB histograms (Red: black line; Green: dashed line; Blue: grey line). (b) Results of CA processing, 231 images pairs were selected (red color points); the blue line describes the correlation value for the mean value of the three RGB bands for all the *n-1* pairs.

results were achieved according to the movement estimation of the glacier. Note that $w = (u; v)^T$ is the optical flow field, i.e., a function $w: \Omega \rightarrow R^2$ where Ω is the image domain, and $w_1(x)$ denotes the correspondence vectors obtained by descriptor matching at some point x (Brox and Malik, 2011).

The first and second terms in Equation 1 represent the common assumption that corresponding image features (points) should have nearly the same gray/black value and gradient. The constraint on the gradient is considered to provide a certain level of invariance to additive changes of brightness that

conditions the matching of the grey/black value. Since both terms are not sufficiently robust for optical flow estimation, a 3rd term is introduced that penalizes the total variation of the optical flow field by a smoothness constraint. Finally, the last two terms help solve the problem of large displacements by combining descriptor matching with the variational model and its coarse-to-fine optimization. The descriptor matching method is based on densely computed Histogram of Oriented Gradients (HOG). The multiscale approach is performed by dividing the original problem into a sequence of sub-problems at different levels of resolution by smoothing the input images. The levels are defined through a pyramid, where levels of resolution (k) are down sampled by a factor of 0.95 (kmax-k), and the kmax is chosen with a discrete derivative filter. Subsequently, the ultimate goal is to find a function *w(u, v)* that minimizes the energy; it is important to mention that the minimization is not a trivial task due to the highly nonlinear model. Brox and Malik (2011) solve this problem by iteratively updated Euler-Lagrange equations using boundary conditions.

Once the flow field is generated by the optical flow method, the flow estimation error is estimated for all pairs. Thereafter, the results are evaluated in a qualitative manner, where the color-coded flow field is used to show the movement of the glacier. Next, based on Steinbrücker *et al.* (2009), the consistency of the flow-field for all image pairs is checked by reconstructing the first image based on the second image using the estimated motion field w according to (Equation 2):

$$I_1^r(\mathrm{x}) = I_2(x+w(x)). \tag{2}$$

If the resultant flow is adequate, then the reconstruction of I_1^r has to be nearly identical to I_1. In order to estimate the error, the absolute difference between the images pairs for the filtered time-lapse image sequence is estimated by computing the mean for each pixel.

To obtain the Total Reconstruction Error (TRE) of the entire period, the reconstruction error value per pair (*REp*) is computed for each pixel over the 231 pairs, and then the error values for two years are estimated by Equation 3. Finally, the scaling model is applied to convert the values to meters.

$$TRE_{axb} = \frac{\sum_{n=1}^{231}\left(\frac{2 * REp_n}{\Delta tp_n}\right)}{\Delta t} \tag{3}$$

where: *axb* is the image size; REp_n is the reconstruction error per pair; Δtp_n is the time difference between the images in an image pair; and Δt is the total time of the study period.

Scaling, Conversion from Image Domain to Object Domain

To obtain the scaled velocity map from the flow field, i.e., to convert motion in image domain to object space, it is necessary to use a DEM to scale the flow parameters at every pixel of the glacier area. DEMs are one of the most common products in the mapping practice and come in a broad range of spatial resolutions and accuracy; although their availability greatly depends on the geographic location. SRTM (Shutter Radar Topographic Mission), one of the most popular global DEMs, has coverage in the Viedma glacier area, and, therefore, it was initially used. Unfortunately the features of the glacier were not well localized due to the low resolution, 30 m grid, against to the about 0.6 m mean Ground Sample Distance (GSD) of the images. Consequently, a sparse DEM based on the 50 GCPs (*p*GCPs and *s*GCPs) was generated to convert the optical flow results in to physical values. In the first step, knowing the ranges between the C1 and each GCP, the GSD values for those GCPs are estimated. Next, using the GCPs an image resampling is performed by a triangulation method, which is an attractive interpolator because it can be adapted to various terrain structures, such as ridge-lines and streams, using a minimal number of data points (McCullagh, 1988). This method generates many flat triangles, and is an exact interpolator (Yilmaz, 2007), and thus was chosen because the glacier area is located in a zone with relevant topographical details. The spatial resolution was calculated for the entire glacier area, and the GSD ranges value from 0.1 m to 0.7 m, the glacier closest and farthest extension in the image, respectively. The Root Mean Square Error (RMSE) between the DEM and GCPs was calculated, and yielded 0.03 m. Figure 4b shows the distribution of the GCPs and resulting DEM generated by interpolation.

Results: Motion Detection

On calving glaciers, the velocities can reach a maximum at the glacier front due to the pulling effect of high calving rates. These effects are, in particular, amplified when near buoyancy conditions at the front are reached by a glacier calving into deep waters (Rivera *et al.*, 2012a). Very little is known about the ice flow velocities near the front of Viedma glacier, and about the ice-lake interactions taking place in this location. In general, ice flow velocities on a valley glacier cross section have maximum values at the center of the valley and decrease down to a minimum at the margins. Along the valley, the ice velocity magnitude varies longitudinally depending on various factors, such as surface slope, mass balance distribution, and the glacier front conditions.

The velocity field at the lower end of the glacier based on the scaled LDOF results is shown in Figure 5a. The velocity

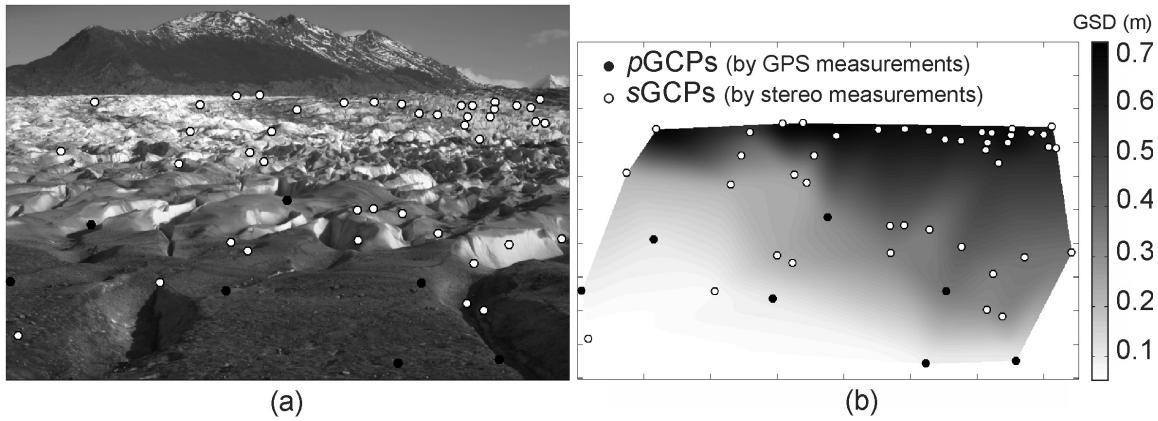

Figure 4. (a) GCP distribution on the glacier surface; GPS surveyed, marked by black dots and photogrammetrically derived ones marked by white dots, and (b) DEM created by triangulation method.

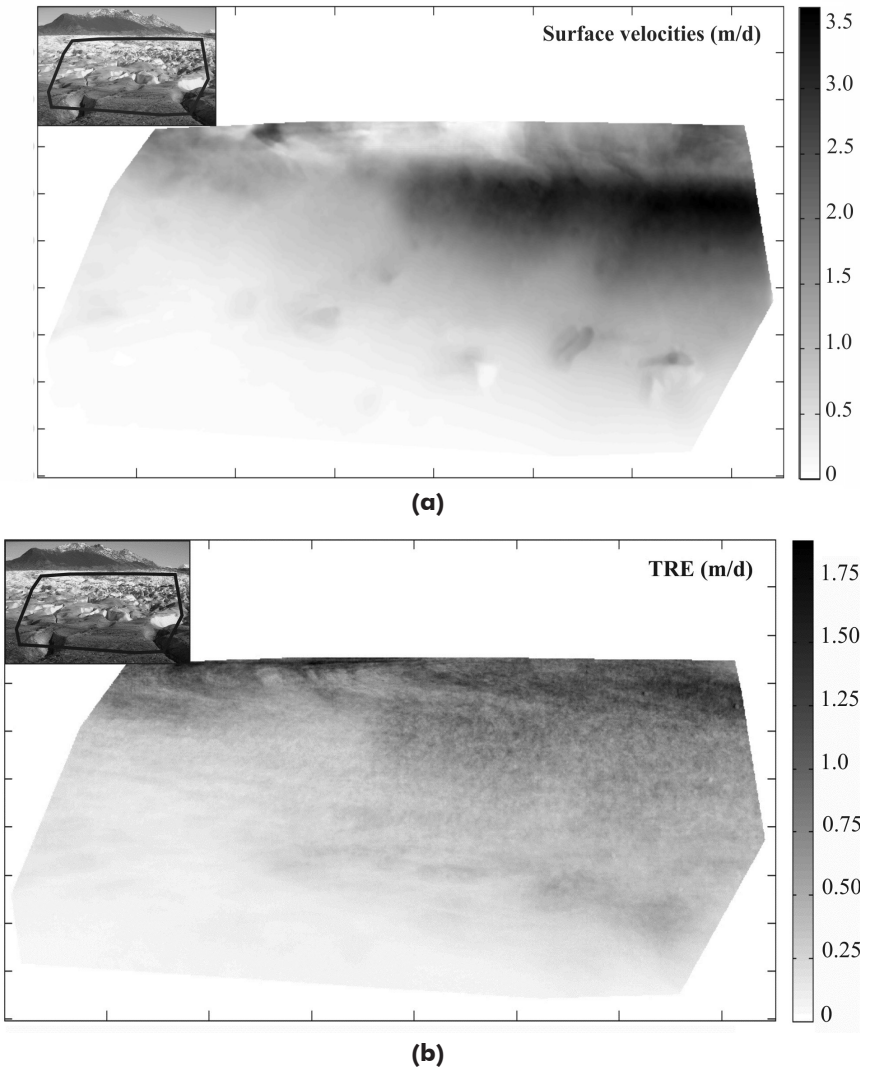

Figure 5. (a) Flow vectors in meters per day (m/d), and (b) Error model based on TRE assessment.

field is calculated from the average magnitudes of 231 image pairs, and the mean surface velocities reach values between 3.5 m/d and 0.5 m/d (meters per day) in the central area and near to the margins, respectively. The fast flow area is mainly concentrated at the central part, pictured in black, while the slow moving ice areas are mainly located toward the margins shown in light grey. This pattern is consistent with the expected ice flow acceleration toward the glacier front central part, and with the slow moving ice near the margins. This near front acceleration has been previously described for other calving glaciers in Patagonia (Sakakibara *et al.*, 2014), where calving is driven by deep water near the front. At the Viedma glacier, this is confirmed by the recently surveyed bathymetry of the lake, where up to 571 m water depths were detected. Note that between April 2014 and March 2016, the central part of the glacier front retreated near 800 m, as detected by satellite images. Former results, obtained by offset tracking Synthetic-Aperture Radar (SAR) imagery between April to June 2012 by Riveros *et al.* (2013) showed values less than 4 m/d at the terminus area. Mouginot and Rignot (2015), using radar and Landsat images between 1994 and 2014, provided surface velocities in the range of 1 and 2 m/d near the end part. Furthermore, we conducted surface velocities estimation of Viedma glacier by LANDSAT images, acquired in October and February 2015, and March 2016, using the feature tracking technique (Lo Vecchio et al., in review). These results at the terminus show similar patterns obtained in the present study, with an acceleration of the front where maximum values reached 2.5 ±0.3 m/d. Therefore, the different values of velocities found in these investigations are reasonably close to each other and can be explained by different sensors and geospatial data acquisition platforms, techniques, creating different spatial and temporal resolution data, plus the algorithms used.

Figure 5b shows the TRE_{axb} for the entire study period, displaying a range from 1.8 m/d until 0.2 m/d. The largest errors are reported for the area located at the glacier surface and mountain border area. In this zone, the computation of the optical flow was less accurate due to the larger object distance; note that the TRE_{axb} mean value reached 0.36 m/d. In addition, based on Equation 2, Figure 6 shows the mean error (grey) for each image pair in the filtered time-lapse sequence (231 pairs), and the standard deviation (black) is shown as error bar only for the large peaks. The average mean and standard deviation are 5.7 ±7.9 in pixels (in the image domain). This graph allows visualizing anomalous pairs used in optical flow computation, despite passing the CA test. The large peaks are closely related to big changes in lightness between the images in an image pair; in almost all cases, there was a presence of clouds in some region, snow cover, and not-uniform melting of the glacier surface, as described by Vogel *et al.* (2012), which affect the motion computation. The velocity estimation can be further refined by applying the constraint of slowly changing velocity; an effect known from glacier dynamics. So applying a low-pass filter and then removing outliers can measurably bring down the standard deviation of the velocity estimation.

Figure 7a and 7b show the reconstructed errors for two examples. The top frames show the images that define the image pair for the LDOF computation. Figure 7a shows a case of changing lighting conditions, resulting in significant errors in the computation of LDOF. Below the left image, the results of the LDOF are shown with color-coding for better visualization (Liu *et al.*, 2011); clearly, very poor optical flow computation performance. Each pixel symbolizes a vector where the magnitude and orientation are the function of the tonality and saturation of the pixel value. Below the right image, the error reconstruction is shown. Note that it is easy to identify the cause of these errors because the objects, such as presence of clouds, changes in snow cover, or shadows over the crevasses, appear and disappear between the images pairs. In contrast, Figure 7b shows an example with good lighting conditions where the error remains low over the entire area. Note the interesting situation in the middle of the frame, where the presence of people is observed, clearly indicating the ability of the LDOF to detect small changes with high precision.

Conclusions

In this work, we have applied dense optical flow field method to estimate glacier movement at high accuracy. The feasibility

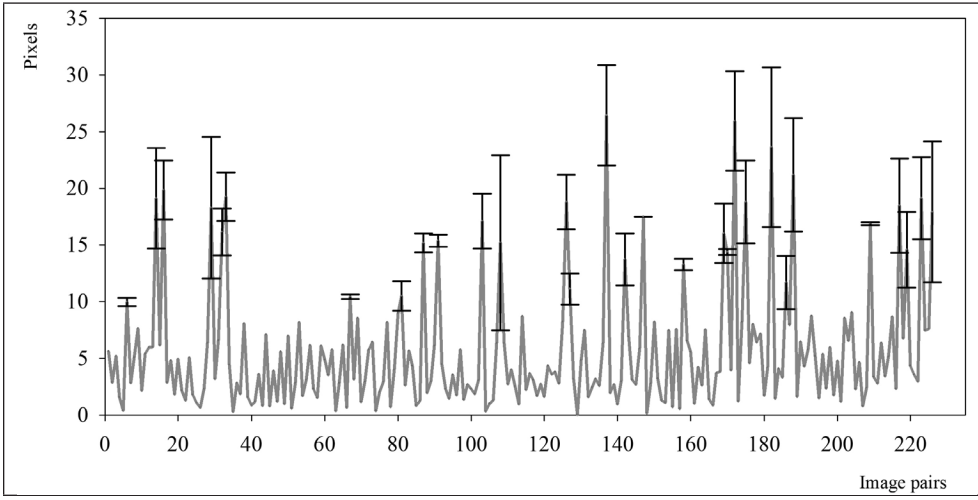

Figure 6. Mean error and standard deviation (error bar) distribution for the image pairs processed by LDOF.

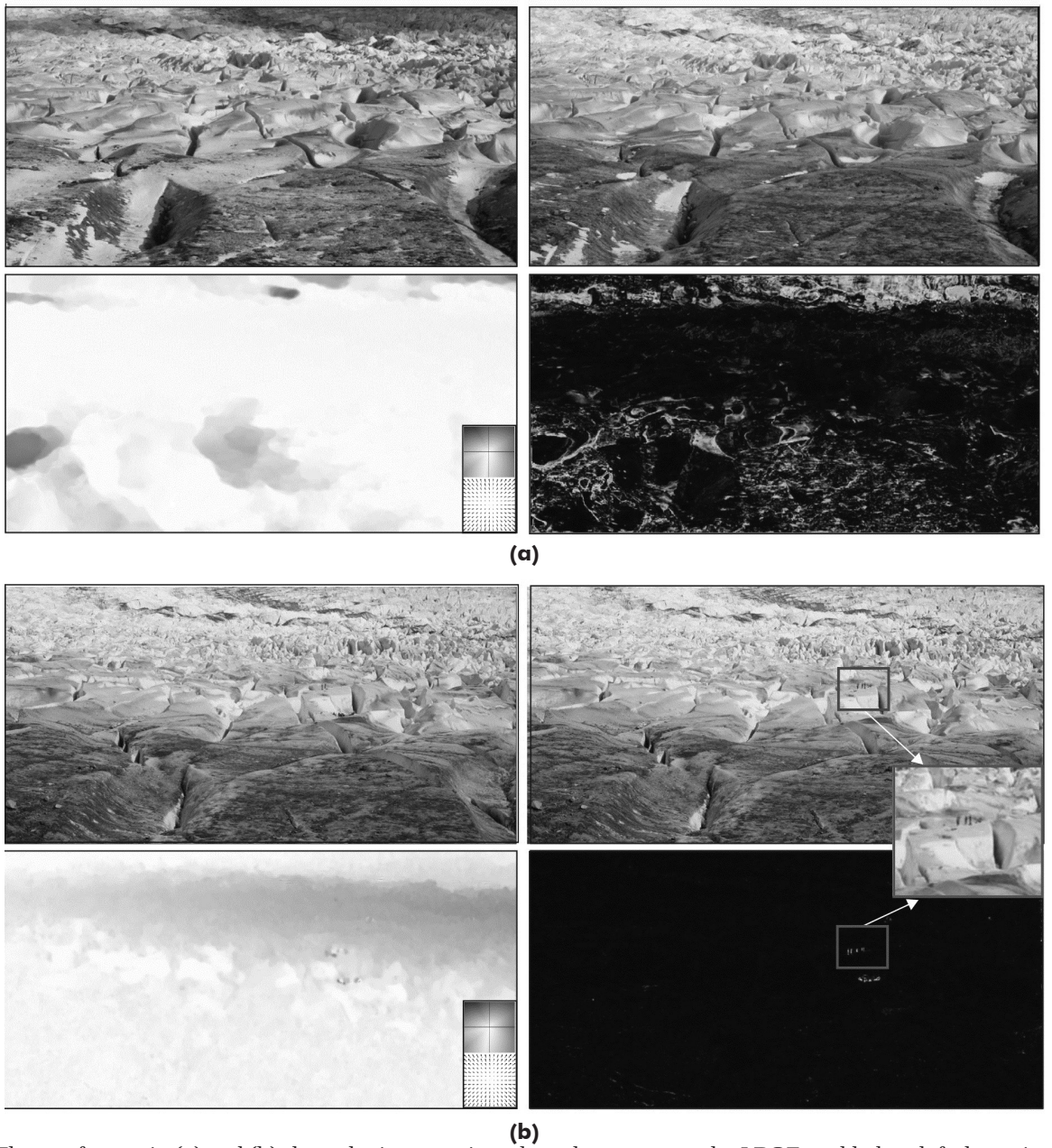

Figure 7. The top frames in (a) and (b) show the image pairs selected to compute the LDOF, and below left the estimated flow field with greyscale-coding for a better visualization; the error reconstruction are shown, respectively. Note that (a) represents a significantly changing lighting condition resulting in poor estimation of the glacier motion, while (b) illustrates good lighting conditions, and although the glacier has a large displacement, yet it is correctly matched.

of the method was tested by using time-lapse imagery obtained at the terminus of the Viedma glacier, SPI, Argentina, by using a 16 Mpixel CANON EOS Mark II DSLR camera. Images were acquired once a day for nearly two years, and preprocessed to correct for sensor modeling errors and then reduced in size to the glacier area. In addition field surveys were conducted acquire ground control (GCP).

The large displacement optical flow (LDOF) method was selected for the investigation. Any optical flow calculation is based on the assumption that change in image intensities are due to changes in object shape, such as deformation or motion; a hard to achieve condition in real life. Therefore, the time-lapse image sequence was filtered to remove images with very different intensity characteristics; mainly, due to varying cloud cover, snow, and weather that may induce rapid melting. The CA method provided a good solution to measure differences between images, and based on our settings, resulted in 38 percent of the images passed the test and were used for subsequent processing. The LDOF algorithm provided optical flow in the image domain by providing a motion vector to all the pixels. To convert the estimated motion to actual velocity values, a sparse DEM was created and triangulation was used for interpolation. Then, based on the DEM, the scaling was estimated and used to convert the results from image domain to object domain. Thus, glaciological analysis and interpretations through the velocity field quantification were obtained.

The resulting glacier surface velocities have reached a maximum value of 3.5 m/d in the central part that is consistent with the expected ice flow of a calving glacier with high velocities near to the terminus. The estimation error was evaluated qualitatively and quantitatively, and the directly computed mean TRE was 0.36 m/d. Factoring in the glacier dynamics, the changes in velocities are slow, and thus, it is fair to say that the mean error is rather conservatively estimated. Larger errors were confined to the farther part of the glacier, where the larger range limited the estimation accuracy. Also, object occlusion is more frequent in these areas, also contributing to larger errors.

In summary, the proposed method based on computer vision and photogrammetric techniques, combining the CA and LDOF algorithms, has shown very good performance at detecting ice flow movement, and ultimately estimating the surface velocity of the Viedma glacier. In addition, the time-lapse sequence provided a good temporal resolution, helping improve the results. Although, no reference data was available for an independent comparison, the limited data from earlier investigations as well as the known glacier behavior are consistent with the obtained velocity estimation results. The data acquisition system is simple and affordable, the selected algorithms provide robust computation, so the overall performance is primarily dependent on the environmental conditions. In the selected test areas, Viedma glacier, about in 40 percent of the time, good quality imagery could be acquired in a two year period, resulting an accurate velocity estimation of the glacier surface.

Acknowledgments

Fieldwork was funded by Grants PICT 2921-2012 and PICT 1995-2013, Agencia Nacional de Ciencia y Tecnología Argentina (ANCyT). The authors would like to thank Adalberto Ferlito, Marcelo Durand, Andrés Lo Vecchio, and Robert Bruce for field assistance. Support from the Los Glaciares National Park is greatly appreciated. Andrés Rivera was supported by FONDECYT 1171832 and CECs

References

Ahn, Y., and J.E. Box, 2010. Instruments and Methods. Glacier velocities from time-lapse photos: Technique development and first results from the Extreme Ice Survey Greenland, *Journal of Glaciology*, 56:198.

Aniya, M., H. Sato, R. Naruse, P. Skvarca, and G. Casassa, 1996. The use of satellite and airborne imagery to inventory outlet glaciers of the Southern Patagonia Icefield, South America, *Photogrammetric Engineering & Remote Sending*, 62(12):1361–1369.

Aniya, M., 2013. Holocene glaciations of Hielo Patagónico (Patagonia Icefield), South America: A brief review, *Geochemical Journal*, 47(2):97–105.

Bamber, J., and A. Rivera, 2007. A review of remote sensing methods for glacier mass balance determination, *Global and Planetary Change*, 59:138–148.

Bartholomé, E., and A.S. Belward, 2005. GLC2000: A new approach to global land cover mapping from Earth observation data, *International Journal of Remote Sensing*, 26(9): 1959–1977.

Beauchemin, S.S., and J.L. Barron, 1995. The computation of optical flow, *ACM Computing Surveys*, 27:433–466.

Benn, D., and D. Evans, 2010. *Glaciers & Glaciation*, Routledge Publishing. New York, 802p.

Bolch, T., A. Kulkarni, A. Kääb, C. Huggel, F. Paul, J.G. Cogley, and S. Bajracharya, 2012. The state and fate of Himalayan glaciers, *Science*, 336(6079):310–314.

Bouguet, J.Y., 2001. *Pyramidal Implementation of the Affine Lucas Kanade Feature Tracker Description of the Algorithm*, Intel Corporation, 5(1–10):4.

Bown, F., 2015. *Dinámica Frontal de un Glaciar de Descarga Oceánica: Glaciar Jorge Montt, Campo de Hielo Patagónico Sur*, Ms. dissertation, Universidad de Concepción, Chile, 104 p.

Brox, T., A. Bruhn, N. Papenberg, and J. Weickert, 2004. High Accuracy optical flow estimation based on a theory for warping, *Proceedings of the 8th European Conference on Computer Vision*, Springer LNCS 3024 (T. Pajdla and J. Matas, editors), Prague, Czech Republic, 4:25–36.

Brox, T., C. Bregler, and J. Malik, 2009. Large displacement optical flow, *Proceedings of the IEEE International Conference on Computer Vision and Pattern Recognition (CVPR)*.

Brox, T., and J. Malik, 2011. Large displacement optical flow: Descriptor matching in variational motion estimation, *IEEE Transactions on Pattern Analysis and Machine Intelligence*, 33(3):500–513.

Chang, C., and S. Chatterjee, 1992. Quantization error analysis in stereo vision, *Signals, Systems and Computers*, October, 1992 Conference Record of The Twenty-Sixth Asilomar, IEEE, pp. 1037–1041.

Clarke, T.A., and J.G.Fryer, 1998. The development of camera calibration methods and models, *The Photogrammetric Record*, 16(91):51–66.

Danielson, B. and M. Sharp, 2013. Development and application of a time-lapse photograph analysis method to investigate the link between tidewater glacier flow variations and supraglacial lake drainage events, *Journal of Glaciology*, 59:287–302.

De la Nuez, A.J.S., 2010. *Métodos Variacionales para la Estimación del Flujo* Óptico *y Mapas de Disparidad*, Universidad de Las Palmas de Gran Canaria, pp. 17–24.

Gao, J., and Y. Liu, 2001. Applications of remote sensing, GIS and GPS in glaciology: A review, *Progress in Physical Geography*, 25(4):520–540.

Garcia Tomaselli, A.M., M.L. Lopes Reiss, 2005. A photogrammetric method for single image orientation and measurement. Photogrammetric Engineering & Remote Sensing, 71(6):727–732.

Gleitsmann, L., and M. Kappas, 2006. Glacier monitoring survey flights below clouds in Alaska: Oblique aerial photography utilizing digital multiple image photogrammetry to cope with adverse weather, *EARSel eProc*, 5(1):42–50.

Granshaw, S.I., and C.S. Fraser, 2015. Computer vision and photogrammetry: Interaction or introspection?, *The Photogrammetric Record*, 30(149):3–7.

Hashimoto, T., M. Kaneko, A. Rövid, S. Isono, T. Sone, K. Baba, A. Fukuda, M. Aniya, N., Naito, H. Enomoto, and P. Skvarca, 2009. An introduction of high-precise 3D measurement system and its applications, *Journal of Automation, Mobile Robotics & Intelligent Systems*, 3(4).

Harrison, W.D., K.A. Echelmeyer, D.M. Cosgrove, and C.F. Raymond, 1992. The determination of glacier speed by time lapse photography under unfavorable conditions, *Journal of Glaciology*, 38(129):257–265.

Heid, T., and A. Kääb, 2012. Evaluation of existing image matching methods for deriving glacier surface displacements globally from optical satellite imagery, *Remote Sensing of Environment*, 118:339–355.

Horn, B., and B. Schunck, 1981. Determining optical flow, *Artificial Intelligence*, 17:185–203.

Howat, I.M., I. Joughin, and T.A. Scambos, 2007. Rapid changes in ice discharge from Greenland outlet glaciers, *Science*, 315(5818):1559-1561. doi: 10.1126/science.1138478.

Kearney, J.K., W.B. Thompson, and D. Boley, 1987. Optical flow estimation: An error analysis of gradient-based methods with local optimization, *IEEE Transactions on Pattern Analysis and Machine Intelligence*, PAMI-9(2):229-244.

Klette, R., 2014. *Concise Computer vision. An Introduction into Theory and Algorithms*, Springer, New Zealand, 429 p.

Kneip, L., D. Scaramuzza, and R. Siegwart, 2011. A novel parametrization of the perspective-three-point problem for a direct computation of absolute camera position and orientation, *Proceedings of the IEEE Conference on Computer Vision and Pattern Recognition (CVPR)*, June, pp. 2969–2976.

Lannutti, E., M.G. Lenzano, C. Toth, I. Lenzano, and A. Rivera, 2016. Optical flow applied to time-lapse images series to estimate glacier motion in the Southern Patagonia Icefield, *ISPRS-International Archives of the Photogrammetry, Remote Sensing and Spatial Information Sciences*, pp. 503–509.

Lenzano, M.G., Lannutti, E., Toth, C., Lenzano, L., Lo Vecchio, A., 2014. Assessment of ice-dam collapse by time-lapse photos at the Perito Moreno Glacier Argentina. ISPRS,The International Archives of the Photogrammetry, Remote Sensing and Spatial Information Sciences, XL-1:11–217. http://dx.doi.org/10.5194/isprsarchives-XL-1-211-2014.

Lichti, D.D., A. Habib, and I. Detchev, 2009. An object-space simulation method for low-cost digital camera stability testing, *Photogrammetric Engineering & Remote Sensing*, 75(12):1407–1414.

Liu, C., 2009. *Beyond pixels: Exploring New Representations and Applications for Motion Analysis*, PhD. dissertation, Massachusetts Institute of Technology.

Liu, C., J. Yuen, and A. Torralba, 2011. Sift flow: Dense correspondence across scenes and its applications, *IEEE Transactions on Pattern Analysis and Machine Intelligence*, 33(5):978–994.

Lopez, P., P. Chevallier, V. Favier, B. Pouyaud, F. Ordenes, F., and J. Oerlemans, 2010. A regional view of fluctuations in glacier length in southern South America, *Global Planetary Change*, 71(1-2):85–108.

Lo Vecchio, A., M.G. Lenzano, M. Durand, E. Lannutti, L. Lenzano, and R. Bruce, Estimation of speed motion and surface temperature from optical satellite imagery at Viedma glacier, Argentina, *Global and Planetary Change*, In review, 2017.

Maas, H.G., G. Casassa, D. Schneider, E. Schwalbe, and A. Wendt, 2010. Photogrammetric determination of spatio-temporal velocity fields at Glaciar San Rafael in the Northern Patagonian Icefield, *The Cryosphere Discussions*, 4:2415–2432.

Matías, J., S.J. Sanjosé, G. López-Nicolás, C. Sagüés, and J.J. Guerrero, 2009. Photogrammetric methodology for the production of geomorphologic maps: Application to the Veleta Rock Glacier (Sierra Nevada, Granada, Spain), *Remote Sensing*, 1:829–841, doi:10.3390/rs1040829.

McCullagh, M.J., 1988. Terrain and surface modelling systems: Theory and practice, *The Photogrammetric Record*, 12:747–79.

Mouginot, J., and E. Rignot, 2015. Ice motion of the Patagonian icefields of South America: 1984-2014, *Geophysical Research Letters*, 42:1441–1449.

Moustafa, A., 2000. Accuracy analysis for new close-range photogrammetric systems, *The International Archives of the Photogrammetry, Remote Sensing and Spatial Information Sciences*, XXXIII, Part B5. Amsterdam, 2000.

Oerlemans, J., 2005. Extracting a climate signal from 169 glacier records, *Science*, 308(5722):675–677.

Piermattei, L., L. Carturan, andA. Guarnieri, 2015. Use of terrestrial photogrammetry based on structure from motion for mass balance estimation of a small glacier in the Italian Alps, *Earth Surface Processes and Landforms*, 40(13):1791–1802.

Rivera, A., M. Koppes, C. Bravo, and J.C. Aravena, 2012a. Little Ice Age advance and retreat of Glaciar Jorge Montt, Chilean Patagonia, *Climate of the Past*, 8:403–414.

Rivera, A., J. Corripio, C. Bravo, and S. Cisternas, 2012b. Glacier Jorge Montt dynamics derived from photos obtained by fixed cameras and satellite image feature tracking, *Annals of Glaciology*, 53(60):147–155.

Riveros, N., L. Euillades, P. Euillades, S. Moreiras, and S. Balbarani, 2013. Offset tracking procedure applied to high resolution SAR data on discussions, Viedma Glacier, Patagonian Andes, Argentina, *Advances in Geosciences*, 35:7–13.

Ryan, J.C., A.L. Hubbard, J.E. Box, J. Todd, P. Christoffersen, J.R., Carr, and N.A. Snooke, 2015. UAV photogrammetry and structure from motion to assess calving dynamics at Store Glacier, A large outlet draining the Greenland ice sheet, *The Cryosphere*, 9:1–11.

Sakakibara, D., and S. Sugiyama, 2014. Ice-front variations and speed changes of calving glaciers in the Southern Patagonia Icefield from 1984 to 2011, *Journal of Geophysical Research: Earth Surface*, 119, doi: 10.1002/2014JF003148.

Schalkoff, R.J., 1989. *Digital Image Processing and Computer Vision: An Introduction to Theory and Implementations*, New York, Wiley, pp. 489.

Schwalbe, E., R. Koschitzki, and H. Maas, 2016. Recognition of drainage tunnels during glacier lake outburst events from terrestrial image sequences, *The International Archives of the Photogrammetry, Remote Sensing and Spatial Information Sciences*, XLI-B8:537–543.

Szelisky, R., 2010. Computer vision: Algorithms and applications, *Springer Science and Business Media*, pp. 957.

Skvarca, P., H. Rott, and M. Stuefer, 1995. Synergy of ERS-1 SAR, XSAR, Landsat TM imagery and aerial photography for glaciological studies of Viedma Glacier, southern Patagonia, *Proceedings of the VII Simposio Latinoamericano de Percepcion Remota*, SELPER, Puerto Vallarta, Mexico, pp.674–682.

Steinbrücker, F., T. Pock, and D. Cremers, 2009. Large displacement optical flow computation without warping, *Proceedings of the 2009 IEEE 12th International Conference on Computer Vision*, IEEE, pp.1609–1614.

Tistarelli. M., 1994. Multiple constraints for optical flow, *Proceedings of the European Conference on Computer Vision*, May, Springer, Berlin, Heidelberg, pp.61–70.

Toth, C., M.G. Lenzano, and L. Lannutti, 2016. Using optical flow to estimate glacier displacements in the South Patagonia Icefield, 16-20 October, *Proceedings of the 37th Asian Conference on Remote Sensing*, Colombo-Sri Lanka, unpaginated CD-ROM.

Toth, C., and G. Jóźków, 2016. Remote sensing platforms and sensors: A survey, *ISPRS International Journal of Photogrammetry and Remote Sensing*, 115:22–36.

Vogel, C., A. Bauder, and K. Schindler, 2012. Optical flow for glacier motion estimation, July, *Proceedings of the 22nd ISPRS Congress, Melbourne, Australia* (25).

Wedel, A., D. Cremers, T. Pock, and H. Bischof, 2009. Structure and motion-adaptive regularization for high accuracy optic flow, September, *Proceedings of the IEEE International Conference on Computer Vision*, pp.1663–1668.

Weinzaepfel, P., J. Revaud, Z. Harchaqui, and C. Schmid, 2013. Deepflow: Large displacement optical flow with deep matching, *Proceedings of the IEEE International Conference on Computer Vision*.

Westoby, M.J., J. Brasington, N.F. Glasser, M.J. Hambrey, and J.M. Reynolds, 2012. 'Structure-from-Motion' photogrammetry: A low-cost, effective tool for geoscience applications, *Geomorphology*, 179:300–314.

Wiśniewski, B., K. Bruniecki, and M. Moszyński, 2013. Evaluation of RTKLIB's positioning accuracy using low-cost GNSS RECeiver and ASG-EUPOS, Transnav, *The International Journal on Marine Navigation and Safety of Sea Transportation*, 7(1):79–85.

Yilmaz, H.M., 2007. The effect of interpolation methods in surface definition: An experimental study, *Earth Surface Processes and Landforms*, 32:1346–1361.